



Article

Deception Island 1967–1970 Volcano Eruptions from Historical Aerial Frames and Satellite Imagery (Antarctic Peninsula)

Gonçalo Prates ^{1,2,3,*} , Cristina Torrecillas ⁴ , Manuel Berrocoso ³ , Gabriel Goyanes ¹ and Gonçalo Vieira ¹

¹ Centro de Estudos Geográficos and Associate Laboratory TERRA, Instituto de Geografia e Ordenamento do Território, Universidade de Lisboa, 1600-276 Lisboa, Portugal

² Instituto Superior de Engenharia, Universidade do Algarve, 8005-139 Faro, Portugal

³ Laboratorio de Astronomía, Geodesia y Cartografía, Departamento de Matemáticas, Facultad de Ciencias, Universidad de Cádiz, Puerto Real, 11510 Cádiz, Spain

⁴ Escuela Técnica Superior de Ingeniería, Universidad de Sevilla, 41092 Sevilla, Spain

* Correspondence: gprates@ualg.pt; Tel.: +351-289-800-100

Abstract: Aerial frames and satellite imagery are widely recognized data sources from which to produce maps. For volcanoes, maps enable the quantification of erupted ash and the destruction caused. The last eruptive sequence on Deception Island was endured from 1967 to 1970. Analogue maps were produced via classical photogrammetric methods with a high degree of human intervention mainly to analyse the volcanic-centres areas only. However, historical aerial frames cover the whole of Deception Island. Structure from motion photogrammetry, a near-automated compilation of digital image processing strategies, minimizes the degree of human intervention to produce orthographic mosaics and digital elevation models from digital aerial frames. Orthographic mosaics were produced from historical aerial frames of 1956 and 1968, and a Kompsat-3 image of 2020. Their shared root-mean-square deviation was 1.8 m and 1.7 m in easting and northing, respectively, at ground control points measured with phase-differential global navigation satellite systems. The digital elevation models were processed with a root-mean-square deviation of 2.3 m and 3.6 m from 1956 and 1968 aerial frames, respectively. As the first application, erupted ashfall and the subsequent destruction, mainly at the former Chilean and British bases, were identified, and the volume of erupted ash was assessed to be over 0.16 km³ within the area mapped by these new digital cartographic products.

Keywords: historical aerial frames; structure from motion; 1967–1970 volcanic sequence; Deception Islands; Antarctic Peninsula



Citation: Prates, G.; Torrecillas, C.; Berrocoso, M.; Goyanes, G.; Vieira, G. Deception Island 1967–1970 Volcano Eruptions from Historical Aerial Frames and Satellite Imagery (Antarctic Peninsula). *Remote Sens.* **2023**, *15*, 2052. <https://doi.org/10.3390/rs15082052>

Academic Editor: Cristiano Tolomei

Received: 6 March 2023

Revised: 7 April 2023

Accepted: 11 April 2023

Published: 13 April 2023



Copyright: © 2023 by the authors. Licensee MDPI, Basel, Switzerland. This article is an open access article distributed under the terms and conditions of the Creative Commons Attribution (CC BY) license (<https://creativecommons.org/licenses/by/4.0/>).

1. Introduction

1.1. Recent Volcanism and Tectonic Surrounding

Deception Island is the most prominent active volcanic centre in the extensional basin between the South Shetland Islands to the northwest and the Antarctic Peninsula to the southeast (Figure 1a). Its central submerged depression of 9 km in diameter opens to the ocean via a single narrow (500 m) and shallow (20 m) channel. Deception Island itself is 15 km in diameter and peaks at Mount Pond at 539 m above sea level (asl) elongated SSE-NNW and Mount Kirkwood at 452 m asl elongated ESE-WNW (Figure 1b).

The South Shetland Islands, apart from Deception Island, are a volcanic arc formed through the former Phoenix Plate subduction under the Antarctic Plate [1–3]. The north-eastwards regional movement of the Antarctic Plate favours the roll-back of the subducted Phoenix slab, creating an extensional basin with an additional left-lateral component that extends to the Antarctic–Scotia Plate boundary [4–6], further assumed to be a marginal extensional basin [7,8] that propagates from that plate boundary southwestward to Deception Island, its southwest limit (Figure 1a). This complex geodynamics is exhibited in the back-arc volcano–tectonic activity that formed Deception Island, evolving from

submarine pillow lavas to subaerial eruptions, mainly strombolian and phreatomagmatic, shield volcano formation and caldera collapse [4,9–12].

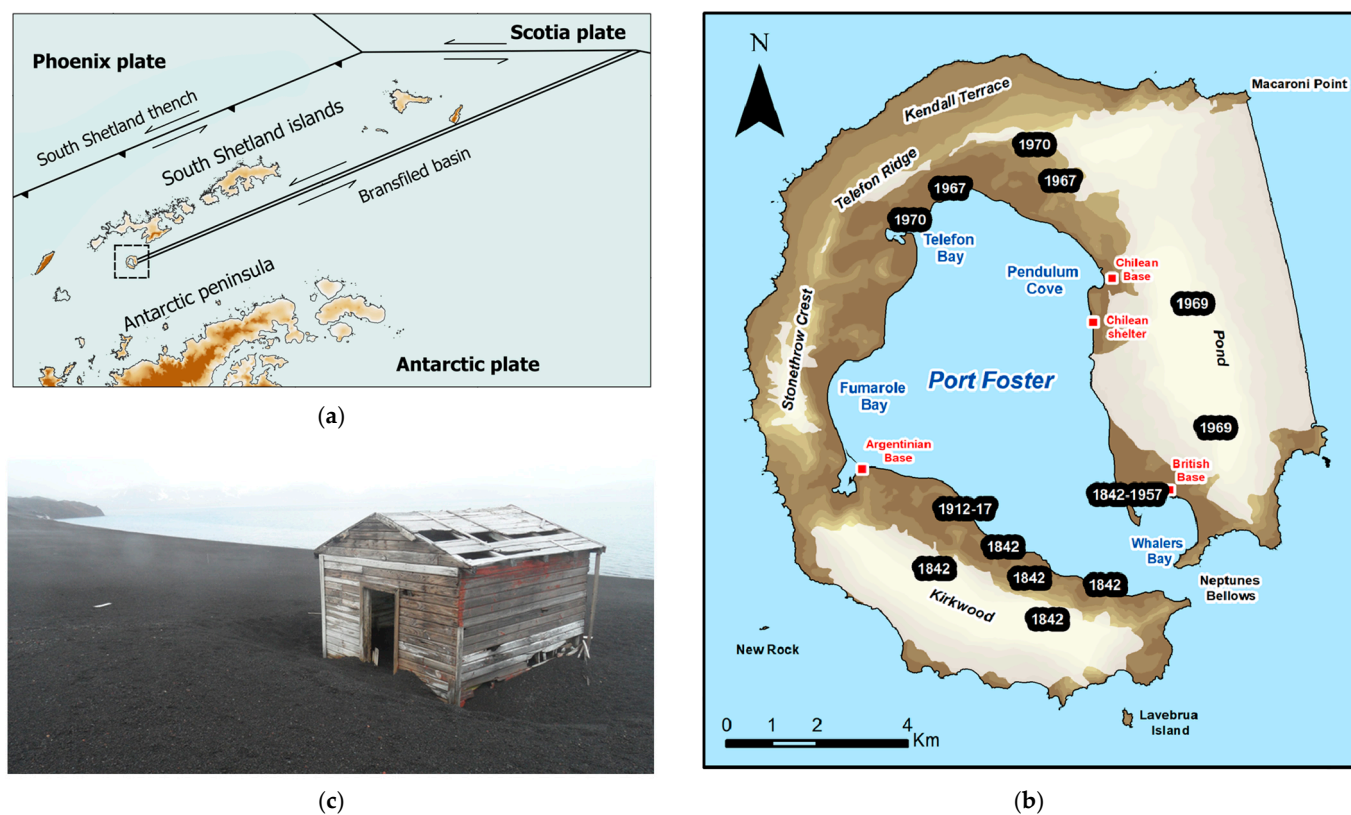


Figure 1. The South Shetland archipelago aligned NE–SW and nearly 100 km north of the Antarctic Peninsula and simplified tectonic surrounding [6] (a). Deception Island horseshoe-shape after the collapse of the caldera beneath sea level, connected to the ocean through a narrow and shallow passage. The location of the source of the 1967–1970 eruptive sequence events (b). Chilean shelter in 2012 still surrounded by ash fall from the 1967–1970 eruptions (c).

Deception has undergone recent volcanic activity, with confirmed eruptions in 1842, 1871, 1912, 1956, 1967, 1969, and 1970 [11,12] of Volcanic Explosivity Indexes 2–3 small-to moderate-volume monogenetic eruptions ($<0.1 \text{ km}^3$) with ash columns rising 10 km asl [13]. Since then, significant seismic activity has been registered, mostly shallow low-energy earthquakes of magnitude 1–2 [14]. Magnitudes 3–4 were also detected in the seismo-volcanic crisis of 1991–1992 and 1998–1999 [15–17]. A detected increase in thermal activity was also recorded in 2012 and 2013 [18], and more than 15 cm/year of volcano inflation in January 2020, forcing the volcano alert level to be raised [19,20], which denotes Deception as a highly active volcano. Further surficial indicators of volcanic activity are gas emissions and soil at 90°C at 107 m asl near Fumarole Bay; gas emissions and soil at 70°C and 100°C in Whalers and Fumarole Bays, respectively; and springs at 45°C and 65°C in Pendulum Cove and Whalers Bay, respectively [21]. Seismic refraction profiles imply that the submerged caldera is underlain by magma storage at a 2 km depth [22,23]. The temperatures of the surface water and chemical composition within the submerged caldera also suggest hydrothermal activity [24].

The 1967–1970 igneous activity was in the north and east sectors (Figure 1b), drastically changing its submerged caldera coastline and destroying the British base in Whalers Bay and the Chilean base in Pendulum Cove due to ash fall and floods [11,24–26]. A significant volume of ash was emitted and deposited on the neighbouring islands, as found in the James Ross ice cap [27] from 1967 and Johnson Glacier on Livingston Island [28] from 1970.

The volume of erupted ash was estimated at between 0.12 km³ [29] and 0.20 km³ [30], and more recently, 0.10 km³ [12].

The 1967 eruption produced four volcanic centres within Telefon Bay aligned NE–SW near the submerged caldera northern coastline, two with ephemeral well-developed scoria cones, briefly known as Yelcho Island, and a maar crater. One more volcanic centre erupted on land eastwards of the previous four, where a large crater was formed [31]. The 1969 eruption generated floods from Mount Pond that reached both Pendulum Cove and Whalers Bay [30,32]. The 1970 eruption in the northern sector developed a new set of volcanic craters with depths ranging from 40 m to 100 m near the 1967 volcanic crater on land, and maar craters near the 1967 volcanic centres at Telefon Bay, which partially destroyed and annexed the ephemeral Yelcho Island to the mainland [31]. The 1970 craters on land, apart from the wider and deeper crater already covered by an alluvial fan, were measured by global navigation satellite systems (GNSS) in 2006 with depths ranging between 13 and 38 m [33]. The volume of erupted ash was estimated at 0.05 km³, 0.03 km³, and 0.04 km³, respectively in the 1967, 1969, and 1970 phases of the eruptive sequence [29].

1.2. Cartographic Products and Imagery of Deception Island

It has been of particular interest to study volcanic geomorphology based on photogrammetry, recovering historical aerial frames taken both vertically and obliquely to the Earth surface [34–36]. Furthermore, unmanned aerial vehicles added particular interest to photographic data in the real-time study of the evolution of eruptions [37,38].

Geomorphological changes at Deception Island were recorded in different historical maps, cartographies, and satellite imagery, which were previously analysed to determine changes in both volume and coastline by overlapping the historical and new cartography [12,31]. In those studies, all cartographic products had a high degree of human intervention across classical stereo-photogrammetric methodologies and analogue-to-digital conversions. In particular, the 1967–1970 eruptive sequence was analysed in analogue maps at a 1:10,000 scale for 1956, 1968, and 1970 [29,31], and was later re-analysed in digital format, also with satellite imagery from 2003 [12]. The analogue maps were produced from aerial frames taken in 1956 by the Falkland Islands and Dependencies Aerial Survey Expedition (FIDASE), and in 1968 and 1970 by the Servicio de Hidrografía Naval Argentino (SHNA) [29,31].

In contrast with classical stereophotogrammetry, the so-called structure from motion (SfM) is a nearly automated compilation of digital image processing strategies that minimises the degree of human intervention to generate both digital elevation models (DEM) and orthographic mosaics from aerial frames [35,39].

On the availability of digital copies of the aerial frames from 1956 and 1968, SfM was applied to produce new digital elevation models and orthographic mosaics of Deception Island at both epochs. Digital cartographic products from the before- and mid-eruption sequences of 1967–1970 were re-analysed together with a Kompsat-3 satellite image from 2020 and the reference elevation model of Antarctica (REMA) 2 m resolution digital elevation model extracted from pairs of submeter resolution satellite imagery acquired from 2009 to 2021 [40]. In addition to these new digital cartographic products covering all of Deception Island, the analysis will focus on the geomorphologic and human-structure changes in the 1967–1970 eruption sequence from historical aerial frames and structure from motion.

2. Methods and Materials

2.1. Structure from Motion and Rational Polynomial Processing

The geometric consistency of stereo-photogrammetric mapping methods has been well known for nearly a century and is entirely suitable for studying topographical changes and geomorphological dynamics [41,42]. Classical stereo-photogrammetry and structure from motion (SfM) produce both surface models and orthographic mosaics from several overlapping images of the Earth's surface. Nonetheless, SfM solves camera position and surface geometry, together with, through the known geometry of the central projection

of photography and highly redundant data from many automatically detected matching features, proportional to surface texture and image resolution, which is identified in several images from different perspectives and preferably with a high degree of overlap [42,43]. Then, by dividing the overlapping images into handy subsets to independently detect and compute additional matching features, massive geometric data over the point clouds is achieved by using multiview stereo (MvS) processing [44]. The SfM–MvS near-automated strategies consist of the identification of features in individual images, the measurement of their coordinates in the camera reference system, and the estimation of camera and feature positions in a non-scaled arbitrary coordinate system. Only with ground control points or known camera centre positions in an appropriate Earth reference system is the three-dimensional surface reconstruction obtained, generating a dense point cloud and, from it, a corresponding surface mesh.

Due to the projection of each feature by a non-vertical line of sight from the camera centre to the feature (central projection), the corresponding pixel position suffers a radial displacement that depends on the feature height and distance from the frame centre. Hence, to generate orthographic mosaics, the radial displacement of each pixel in the images needs to be corrected, requiring camera positions and surface mesh. Therefore, image processing can be carried out with manual intervention limited to the identification of ground control points.

In addition, to correct the radial displacement of each pixel of satellite imagery, the sensor geometry, position, and surface model must be obtained to deliver an orthographic image. In satellite imagery, the radial displacement is found along each line set, since it is acquired by adjacent sequences of pixel-line sets. Further, rational polynomial coefficients (RPC) models are commonly applied to describe the acquisition process of optical satellite sensors without needing a camera geometry model. The RPC model relates three-dimensional surface coordinates to image coordinates as a ratio of cubic polynomials, whose coefficients are provided with each satellite image and enhanced through ground control points [45,46]. Only corrected orthographic images can be compared to detect geomorphological changes, as can reconstructed surfaces or digital surface models. Surface reconstruction is not obtainable from satellite single images, and so only their orthographic representation can be applied to quantify geomorphological changes.

2.2. Historical Aerial Frames and Satellite Imagery

Three sets of stereo pairs of aerial frames and one single satellite image of Deception Island were analysed (Table 1). In late 1956, split by two days, two sets of 40 and 22 aerial frames were taken by a Fairchild metric camera with a lens focal distance of 152.87 mm, the first at about 3960 m and the second at about 4390 m of flight altitude, with 1:26,000 and 1:28,800 scales, respectively [31]. In 1968, the third set of 30 aerial frames was taken by a K-17 metric camera with a lens focal distance of 152.4 mm and a flight altitude of about 4270 m with a frame scale of 1:28,000 [31]. In analogue-to-digital conversion, the resolution was about 1016 dpi or about 0.02 mm of pixel length, an accepted panchromatic-film grain resolution [47], representing roughly 0.6 m on the Earth's surface at these frame scales. The single satellite image was taken on 09 February 2020 by the Kompsat-3 sensor, with a pixel length resolution of about 0.7 m in panchromatic. Hence, all digital images have similar estimated resolutions. Additional data were accessed from the reference elevation model of Antarctica (REMA) 2 m resolution digital elevation model. REMA was produced from several individual stereoscopic digital elevation models obtained from submeter resolution satellite imagery pairs acquired from 2009 to 2021, and vertically registered to satellite altimetry measurements with absolute submeter uncertainties and relative uncertainties of decimetres [40]. The REMA model was corrected of a geoid height of 19.9 m [48] to obtain heights above sea level.

Table 1. Applied imagery material information.

| Proprietary | Type and Details | Number of Frames/Images | Altitude and Scale | Date |
|---|--|-------------------------|--------------------|------------------|
| The Falkland Islands and Dependencies Aerial Survey Expedition (FIDASE) | Fairchild metric camera f: 152.9 mm | 40 | 3960 m 1:26,000 | December 1956 |
| | | 22 | 4390 m 1:28,800 | December 1956 |
| Servicio de Hidrografía Naval Argentino (SHNA) | K-17 metric camera f: 152.4 mm | 30 | 4270 m 1:28,000 | January 1968 |
| Kompsat-3 | Panchromatic Four bands f: 8600.0 mm | 2 | 685,000 m | 19 February 2020 |

Ground control points, available in the SIMAC geodatabase [49], were measured on Deception Island by phase-differential GNSS for decimeter-level precision in 2002, largely in human structures, thus reducing the ambiguity in their identification. A subset of those points was selected considering that the impact of their precision on the reference frame rotation and the horizontal scale is inversely proportional to the distance between them, as longer distances impose a greater constraint on reference frame rotation and scale. To constrain the vertical scale in the aerial frame processing by SfM, ground control points must also help define the maximum height difference. Hence, eight ground control points were used in all orthographic mosaics to minimize reference frame bias when differentiating them. Two ground control points were added to the aerial frame processing by SfM to constrain the vertical scale and northern outer coastline, which were measured on the orthographic mosaic generated from the satellite images with the REMA digital elevation model. In total, ten ground control points and their coordinates in the World Geodetic System 1984 reference system with Universal Transverse Mercator projection at fuse 20 South (WGS84-UTM20S) were applied to produce the complete set of orthographic mosaics.

Satellite images were processed with their rational polynomial coefficients and the REMA digital elevation model together using ENVI 5.0 software. Stereo pairs were processed using PhotoScan 1.0 software with SfM-MvS strategies. Apart from a few statistical parameters, the ground control point identification was the main human intervention in image processing, and the major source of error. Both sets of stereo pairs for 1956 were processed together, increasing the degree of overlap and enhancing the dense point cloud resolution and, consequently, the digital elevation model precision. However, only the set of stereo pairs without clouds generated the 1956 orthographic mosaic (Figure 2). A matching strategy was executed for the 1968 orthographic mosaic, complementing the stereo pairs of that epoch with those of 1956 without clouds in areas that were geomorphologically unchanged by the 1967 eruption, to raise the degree of overlap and digital elevation model precision, upon which the 1968 orthographic mosaic was based and generated (Figure 3).

The Kompsat-3 2020 multispectral satellite images were orthorectified and pan-sharpened with their rational polynomial coefficients and the REMA digital elevation model of 2 m resolution. The generated orthographic mosaics showed a systematic positioning error of about 18 m to the southeast relative to the eight ground control points (Figure 4), which were added to the satellite imagery processing. The eight ground control points were adjusted with a mean rms of 1.2 m and 1.0 m in easting and northing, respectively.

Historical aerial frames were then processed, both sets of 39 and 21 stereo pairs from 1956 together, totalling 62 frames. From the previous satellite orthographic mosaic and the REMA digital elevation model, another two ground control points were identified, measured, and included in the SfM processing to add a constraint to the vertical scale and northern outer coastline. In total, ten ground control points (Figure 4) were applied to produce a dense point cloud and a digital elevation model (Figure A1) with an estimated

resolution of 2.7 m and the orthographic mosaic. The mean rms of the ten ground control points were 2.1 m, 1.7 m, and 2.3 m in easting, northing, and height, respectively.

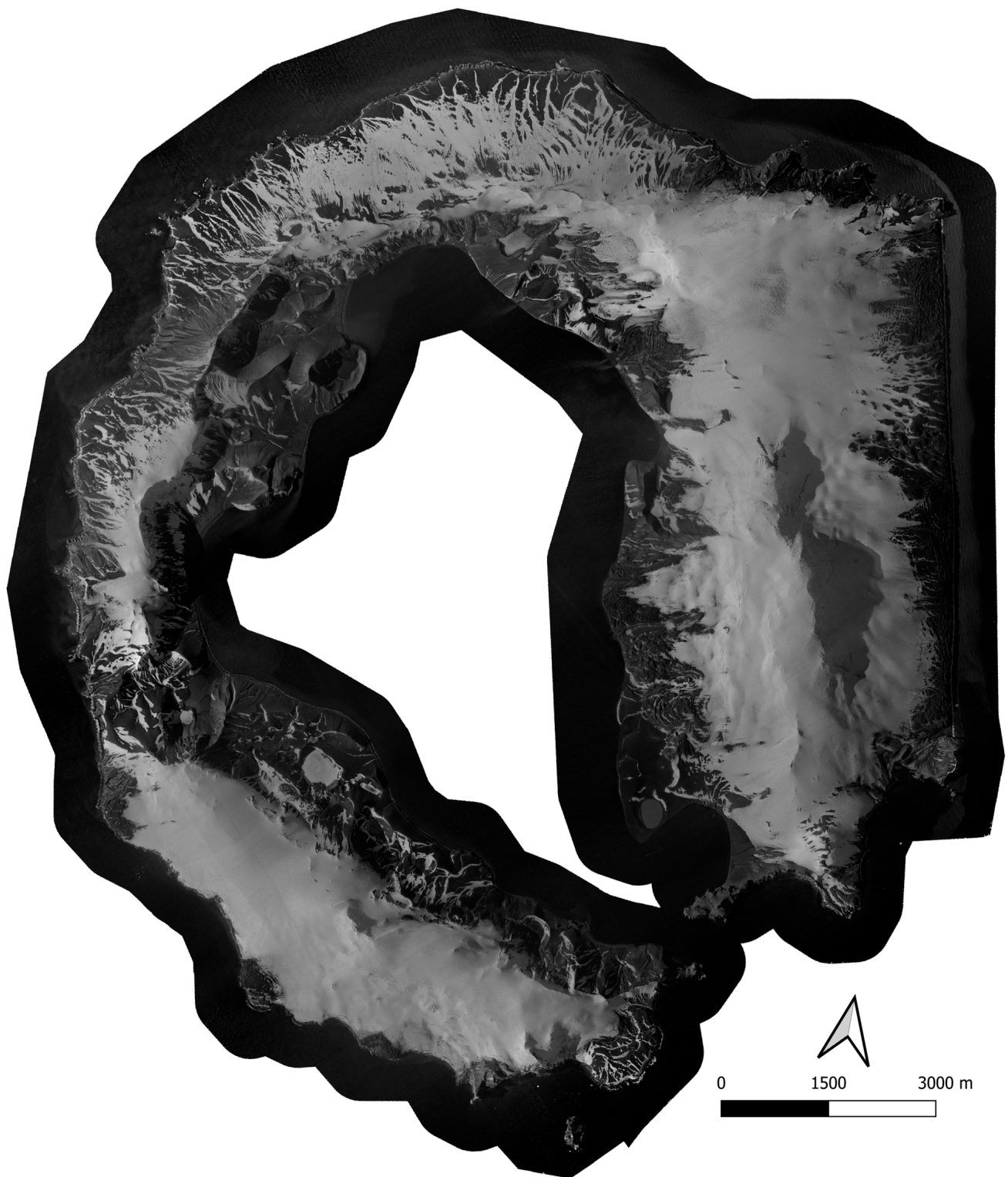


Figure 2. Orthographic mosaic of 1956, before the 1967–1970 eruptive sequence, in black and white, corrected with the computed digital elevation model using SfM–MvS strategies. Both sets of stereo pairs from 1956 were processed together, increasing the degree of overlap and enhancing the dense point cloud resolution and digital elevation model precision. However, only the historical aerial frames set without clouds were used to generate this 1956 orthographic mosaic.

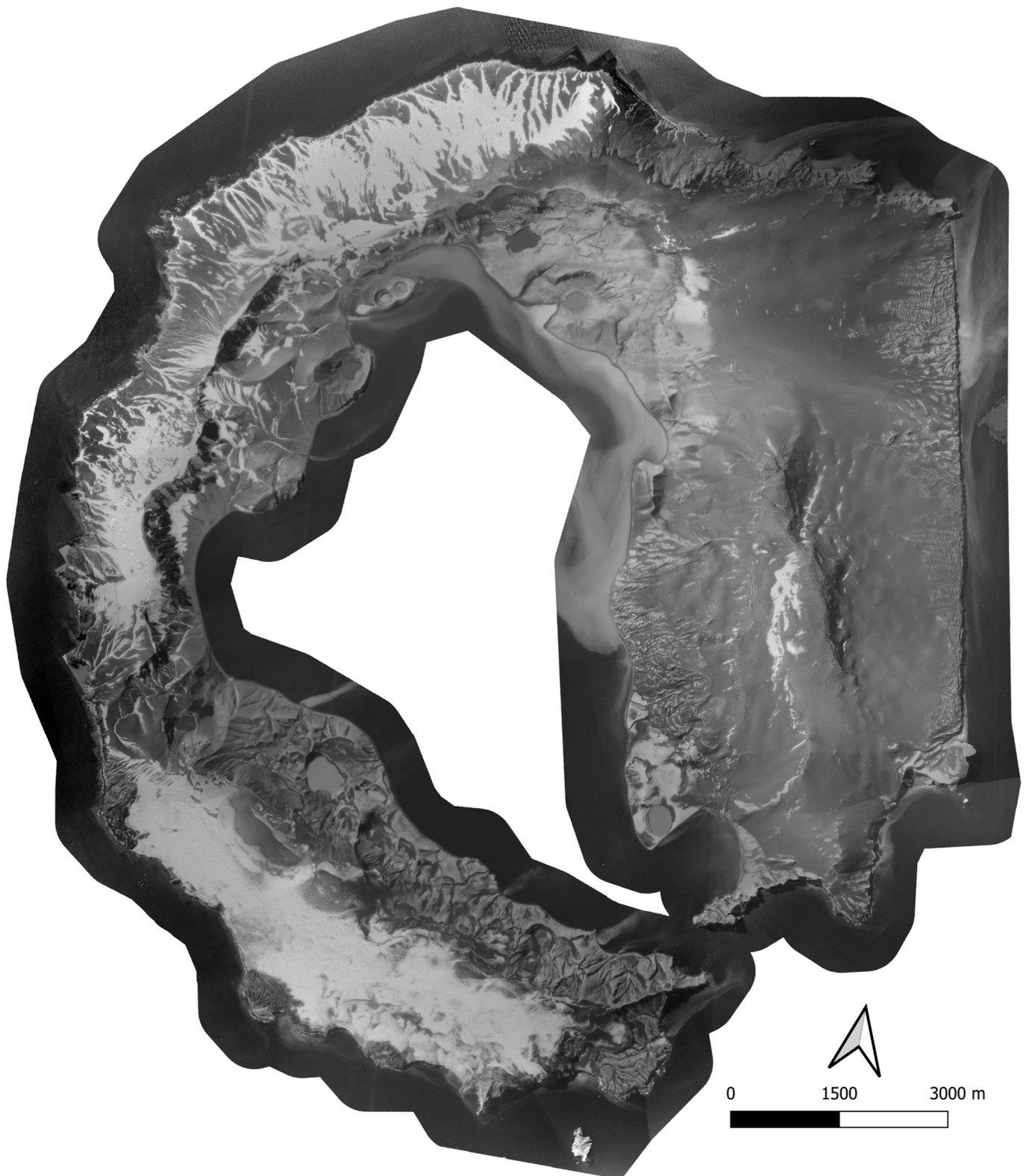


Figure 3. Orthographic mosaic of 1968 after the 1967 eruption ended, in black and white and corrected with the computed digital elevation model using SfM–MvS strategies. The 1968 stereo pairs were supplemented by those from 1956 without clouds in areas geomorphologically unchanged by the 1967 eruption, raising the degree of overlap and digital elevation model precision, which, together with the historical aerial frames of 1968, generated this orthographic mosaic.

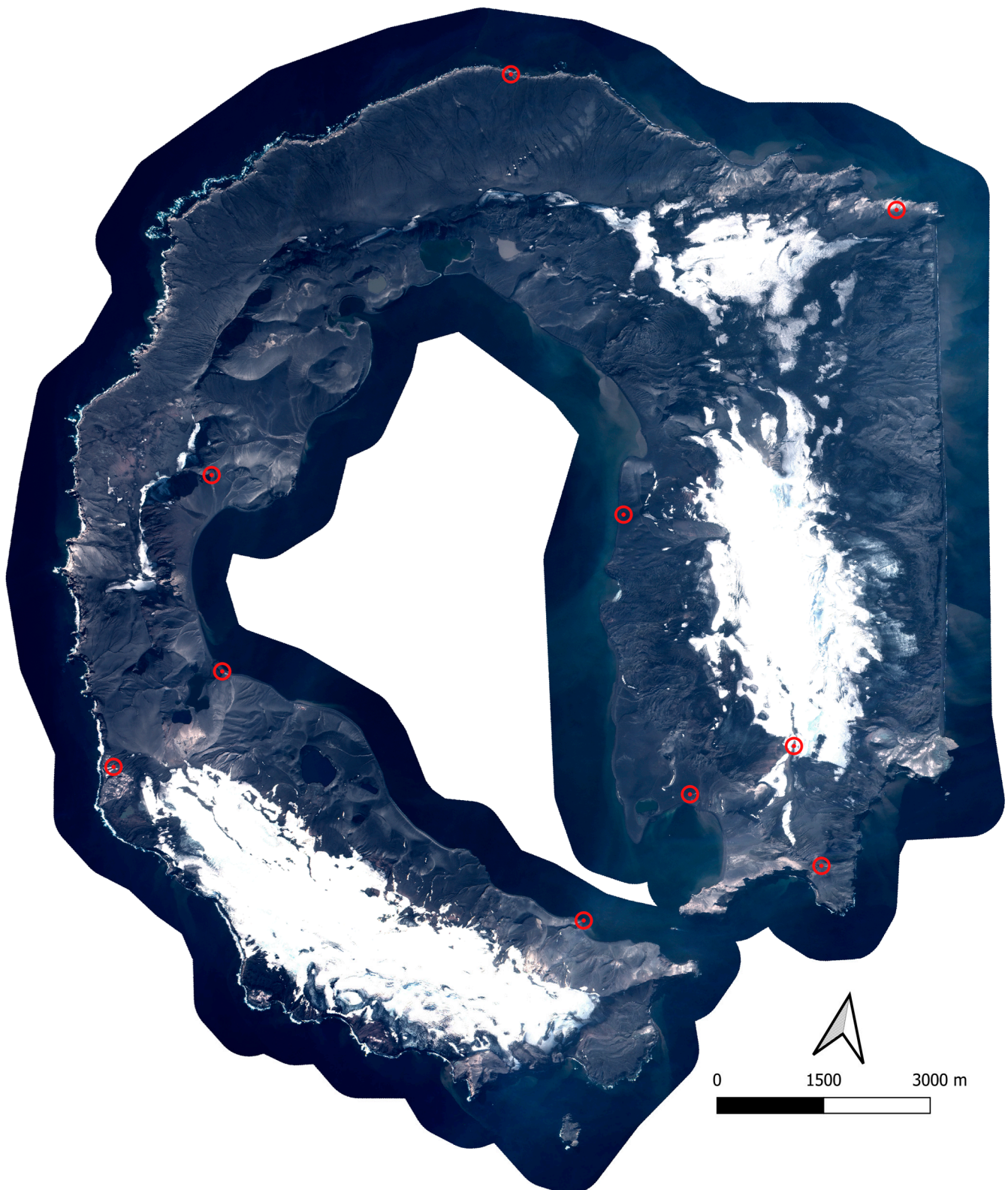


Figure 4. A colour, pan-sharpened orthographic mosaic of 2020 from Kompsat-3 imagery corrected with their rational polynomial coefficients and REMA digital elevation model. The locations of ten ground control points were applied in the production of the orthographic mosaics, as identified inside the red circles. Included material is ©KARI 2020, copyrighted distribution (SI Imaging Services, Republic of Korea), all rights reserved.

The same strategy was applied to the 1968 historical aerial frame processing. Here, the set of 29 stereo pairs from 1968 was supplemented with 21 stereo pairs from 1956 on areas geomorphologically unchanged by the 1967 eruption, totalling 50 frames. The same ten ground control points (Figure 4) were applied in the SfM processing that generated a dense point cloud and a digital elevation model (Figure A1) with an estimated resolution of 2.7 m and the orthographic mosaic. The mean rms of the ten ground control points were 2.3 m, 3.0 m, and 3.6 m in easting, northing, and height, respectively.

3. Results

3.1. Accuracy Assessment of New Digital Cartographic Products

Furthermore, to assess the accuracy of the orthographic images, several other ground control points measured by phase-differential GNSS were also assessed, in particular those of human structures, avoiding the ambiguous identification of natural features, steep terrain, shadows, and snow. Fifty-eight ground control points at the Argentinean (Figures 5 and 6), British (Figures 5 and 7), and Chilean (Figure 8) bases, in spread locations on Deception Island's inner coastline (Figure 1b), had their GNSS coordinates differenced from those measured at their features identified in every orthographic image, and their coordinates' rms was computed. The overall rms of the orthographic mosaics with respect to the phase-differential GNSS was 1.8 m and 1.7 m in easting and northing, respectively (Table A1).

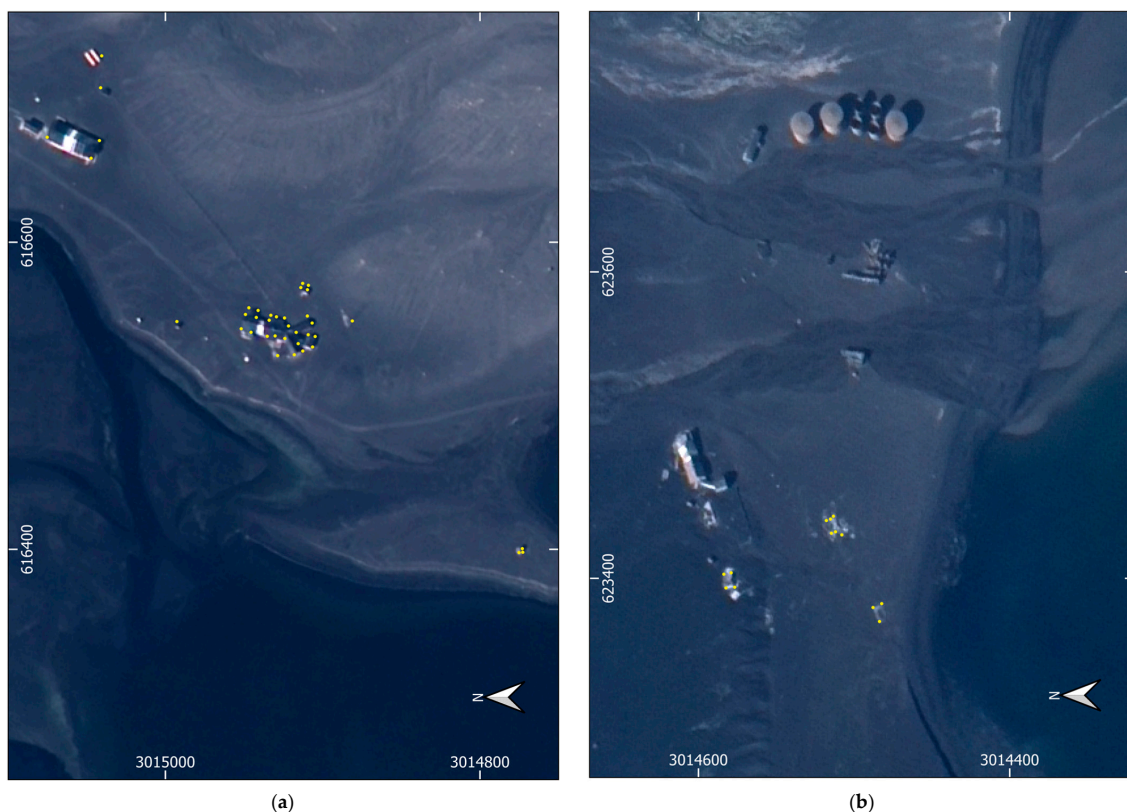


Figure 5. Argentinean (a) and British (b) bases in 2020. Ground control points are coloured yellow, coinciding with the corresponding features, in WGS84–UTM20S. Includes material ©KARI 2020, copyrighted distribution (SI Imaging Services, Republic of Korea), all rights reserved.

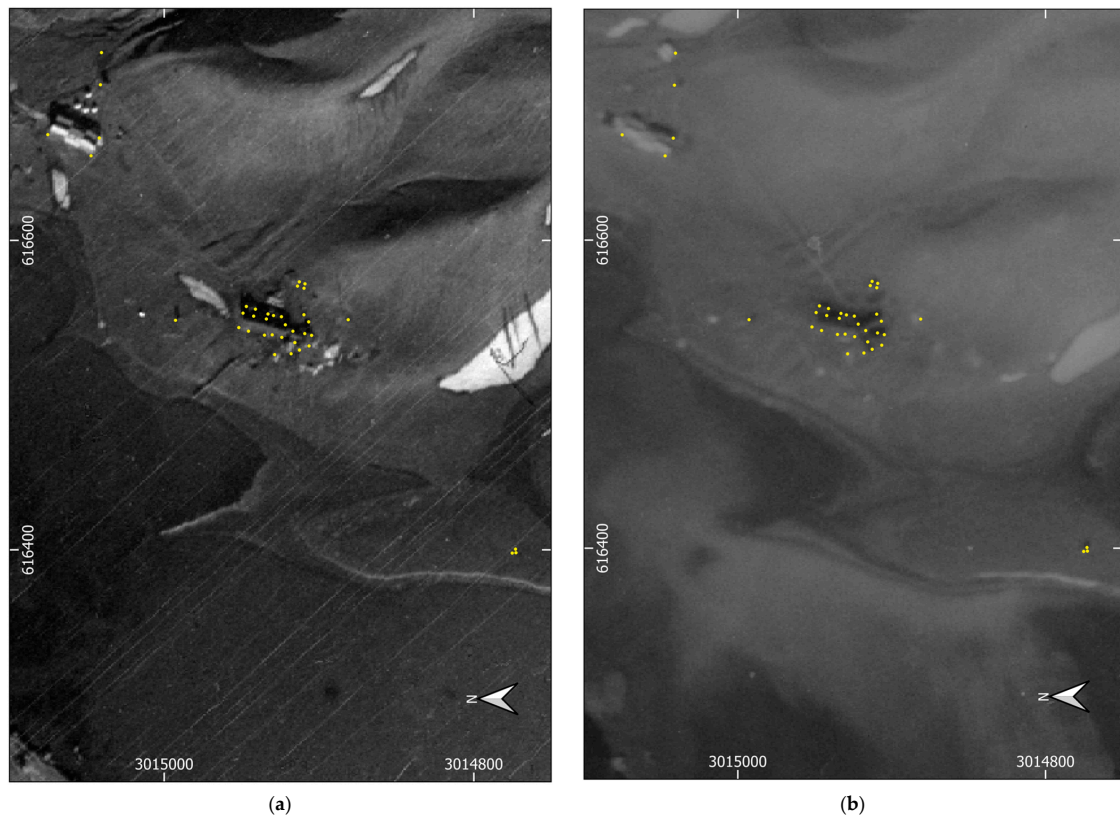


Figure 6. Argentinean base in 1956 (a) and 1968 (b). Ground control points are coloured yellow, coinciding with the corresponding features, in WGS84–UTM20S.

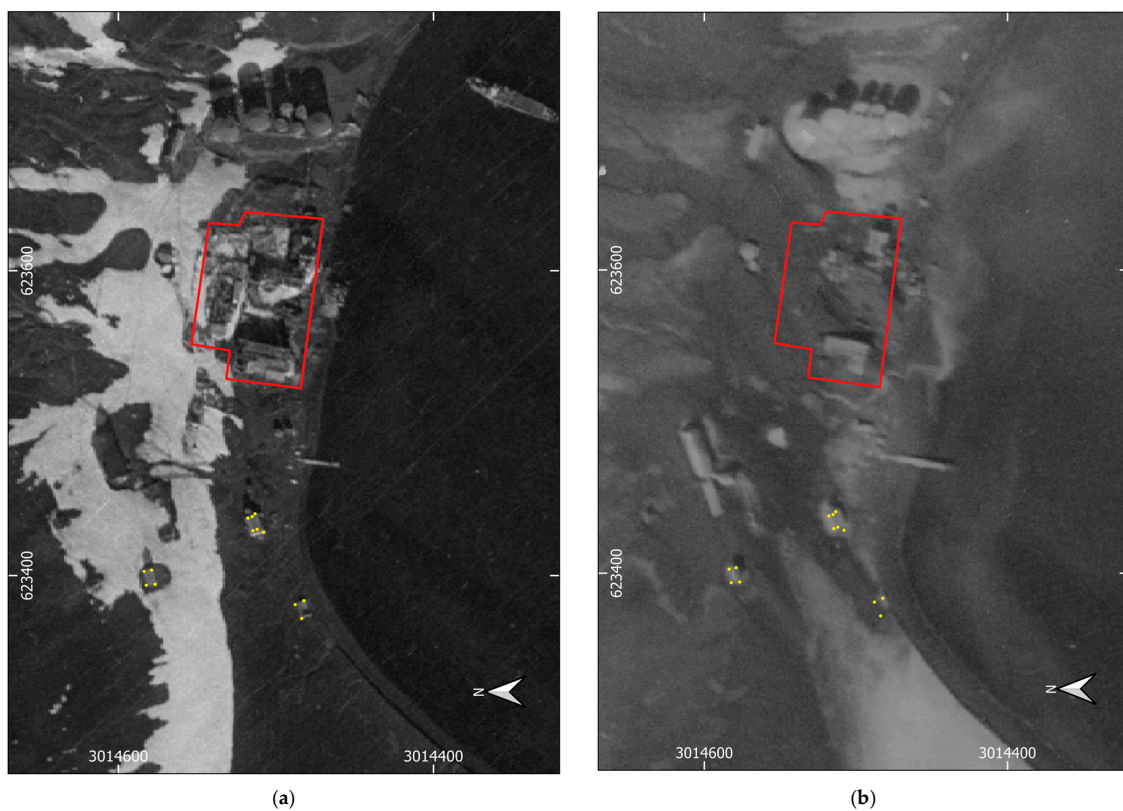


Figure 7. British base in 1956 (a) and 1968 (b). Ground control points are coloured yellow, coinciding with the corresponding features, in WGS84–UTM20S, and red polygon delimiting the main building.

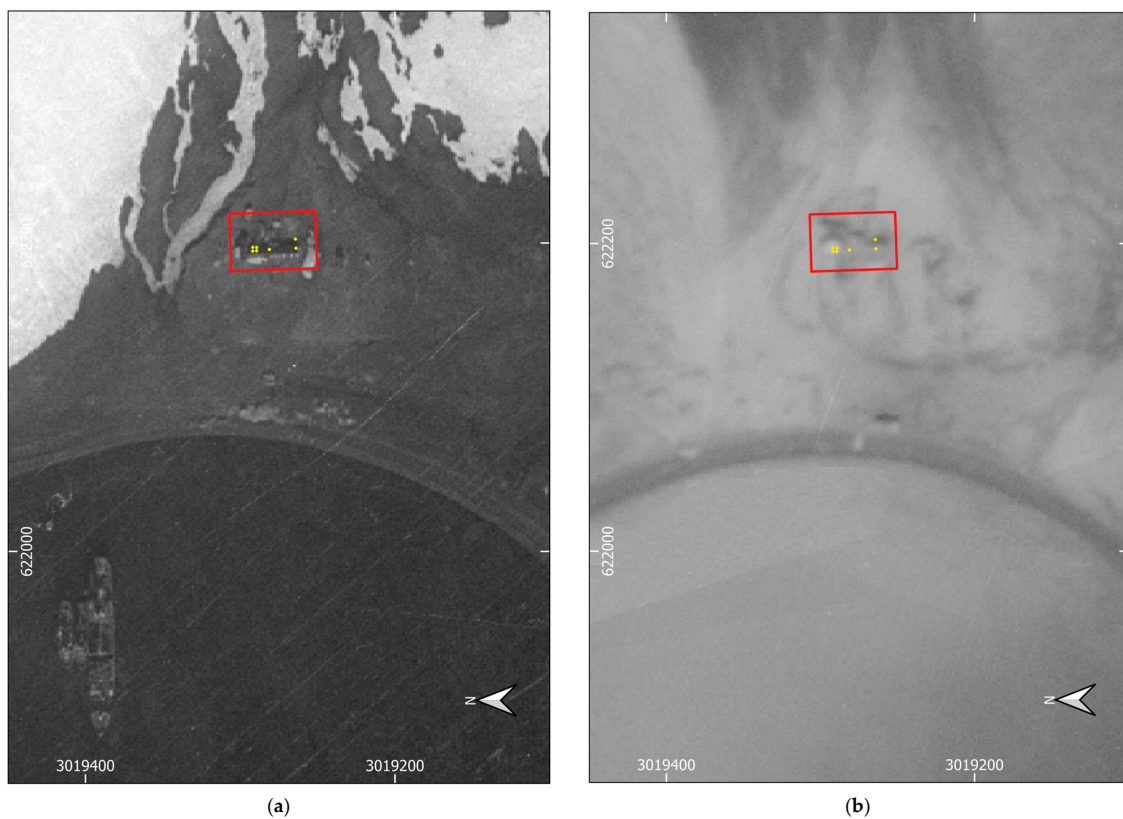


Figure 8. Chilean base in 1956 (a) and 1968 (b). Ground control points are coloured yellow, coinciding with the corresponding features, in WGS84–UTM20S, and red polygon delimiting the main building.

Therefore, horizontal differences should be statistically significant with a 95% confidence level above 4.8 m and should be lower in features with expected immobility. Height differences should be statistically significant with a 95% confidence level above 8.4 m between the 1956 and 1968 digital elevation models and above 7.4 m between the 1968 and REMA digital elevation models, given the submeter uncertainties of the REMA [40]. Therefore, geomorphological, man-made structure, and biological changes can be found and measured with metric-level accuracy from these orthographic mosaics generated using near-automatic strategies in the processing of these historical aerial frames and satellite imagery.

3.2. New Digital Cartographic Products Historical Aerial Frames Based

From the orthographic mosaics, the destruction of the British (Figure 7) and Chilean (Figure 8) bases is shown, and no major consequence at the Argentinean base apart from ash cover (Figure 6). While the Chilean base's main and only building collapsed, at the British base, the destruction of its central complex of buildings is visible. The ashfall covered the Chilean and Argentinean base man-made structures, although they are still identifiable after the 1967 eruption, the Chilean base being less so. The thickness of ashfall at these locations is compatible with the 3 to 5 m reported [50]. The Argentinean base living building (where ground control points were concentrated) was about that height and is almost completely covered in 1968 (Figure 6b). The Chilean base is similarly covered, depicting the presence of a local elevation at the building location in 1968 (Figure 8b). The British base has less ashfall, depicting a similar height to that at the Chilean shelter, about 0.5 m (Figure 1c) since buildings were not covered; however, several man-made structures are no longer present in 1968 (Figure 7b).

As a consequence of the 1967 eruption, several geomorphological changes are also visible, such as the emplacement of two well-developed scoria cones, which forms an ephemeral small island, briefly known as Yelcho, and one maar crater aligned NE–SW at

Telefon Bay and a prominent crater on land to the east. Those were the major volcanic structures that emerged then (Figure 9), emitting ash that covered the inner coast and all of Mount Pond (Figure 3) [30]. In fact, the exterior coast sheltered by the Kirkwood, Telefon, and Stonethrough ridges suffered minor to no ash fall. As the Mount Pond ridge altitude is higher than the Kirkwood, Telefon, and Stonethrough ridges, the ashfall pattern must be justified by wind direction mainly from the NW at the time of the 1967 eruption [30].

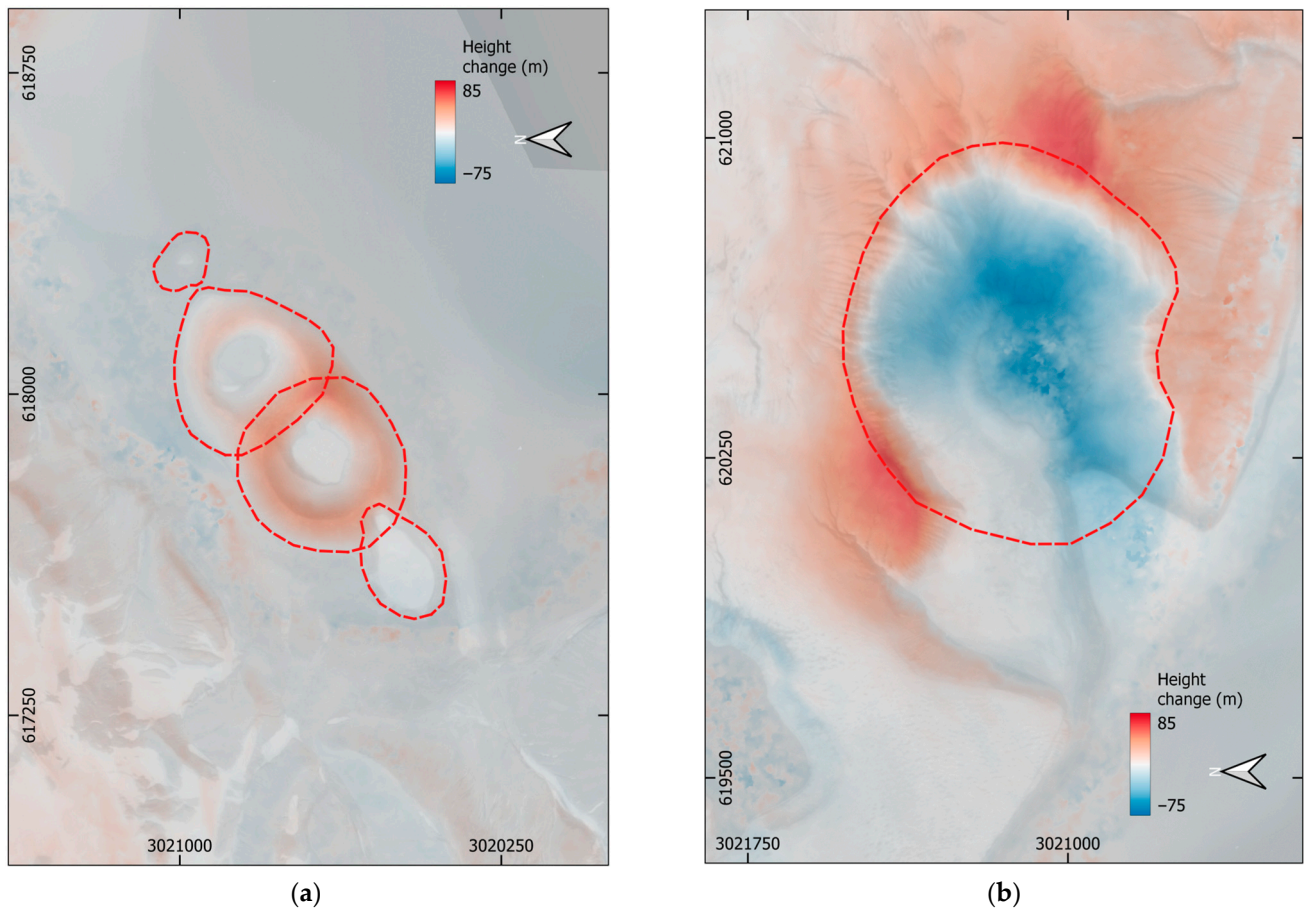


Figure 9. The composition of the orthographic mosaic of 1968 in black and white, overlapped with 30% transparency to the height differences between the 1956 and 1968 digital elevation models in colour from WGS84–UTM20S, and red dashed lines delimiting the main volcanic structures. Well-developed scoria cones and craters in Telefon Bay (a). The crater formed on land with a depth of about 151 m and a diameter of about 600 m (b).

4. Discussion

4.1. The 1967–1970 Eruptive Sequence: 1967 Phase

Based on the generated digital elevation models of 1956 and 1968, and the retrieved REMA digital elevation model averaged between 2009 and 2021, the volume was automatically calculated. Two well-developed scoria cones formed after the 1967 eruption at the northern inner coast at Telefon Bay (Figure 9a) that reached about 33 m, 53 m, and 19 m in height, respectively, the southwest, the in between scoria cones and the northeast rims of the ephemeral Yelcho Island. The volume of erupted ash above sea level in the area defined by Figure 9a was about 0.009 km³. However, for the typical depth of 10 m to 20 m of Deception Island's submerged caldera bays [51], the volume of erupted ash increases by at least 0.003 km³ to 0.006 km³ under the scoria cones above sea level.

A crater formed to the east (Figure 9b), with the central depression deepening by about 79 m and the surrounding rim rising by about 67 m, forming a crater of 151 m in depth. The volume of excavated erupted ash was about 0.017 km^3 while the volume of ashfall around the crater was about 0.028 km^3 . The sum of all of the erupted ash in these two areas was about 0.056 km^3 .

However, the ashfall that covered the inner coast and Mount Pond (Figure 3) that was deposited from an eruptive column of 11 km in height, was not accounted yet. From the ashfall pattern on Deception Island, the estimated area covered by ashfall on the orthographic mosaic of 1968 was about 103.6 km^2 . Considering at least an average thickness of 1 m of ashfall for the area covered on Deception Island, which includes its submerged caldera, this adds a volume of about 0.104 km^3 to the 1967 eruption, although the thickness was reported to be about 3 to 5 m [50].

4.2. The 1967–1970 Eruptive Sequence: 1970 Phases

The 1970 phase of the 1967–1970 eruptive sequence was analysed similarly. The 1970 maar and land craters near the volcanic structures formed during the 1967 eruption were the main volcanic structures uncovered by glaciers. In 1969, there were floods from sub glacier eruptions at Mount Pond, which reached and washed up the Chilean and British (Figure 5b) bases [32], and the volume of erupted ash could not be estimated on these new cartographic products. Although land gained after 1968 to the submerged caldera bays near the Chilean and British bases is depicted in the orthographic mosaic of 2020, in a total volume of 0.002 km^3 and 0.001 km^3 to fill the typical caldera bays of about 20 m in depth [51], according to these products those volumes cannot be attributed to the 1969 floods. In fact, they should be attributed to alluvial fans from Mount Pond instead as these coastlines did not change much until 1970 [12,31].

In 1970, maars helped annex the ephemeral Yelcho Island and the collapse of the northwest faces of the two scoria cones, leaving only their southeast faces (Figure 10a). The volume of erupted ash above sea level in the area defined by Figure 10a was about 0.016 km^3 , while the collapse of the northeast faces of the ephemeral Yelcho Island excavated a volume of 0.003 km^3 . Below the water level, the erupted ash from the six maar craters implies additional volumes of 0.008 km^3 to 0.016 km^3 , respectively, for a 10 m to 20 m depth in Telefon Bay [51].

The eruptive sequence also created seven partially overlapping volcanic craters north of the 1967 crater (Figure 10b). Apart from the major crater covered by an alluvial fan in the 2020 orthographic mosaic and REMA digital elevation model, the uncovered set of craters' central depression deepened to about 60 m, and the surrounding ridge raised by about 25 m, producing a maximum crater' depth of about 85 m. The eruption excavated about 0.011 km^3 of ash and deposited the same amount around the new craters in the area of Figure 10b. Craters from the 1967 and 1970 eruptions have been covered by an alluvial fan throughout the years. In fact, the crater with a depth of about 100 m and a diameter of about 300 m [31] northeast of those visible in the 2020 orthographic mosaic is completely filled, and both of the remaining craters from the 1967 and 1970 eruptions have had their northeast ridges cut, with the alluvial fan moving in. These observations should account for the underestimation in the volume of 0.049 km^3 for the 1970 eruptions.

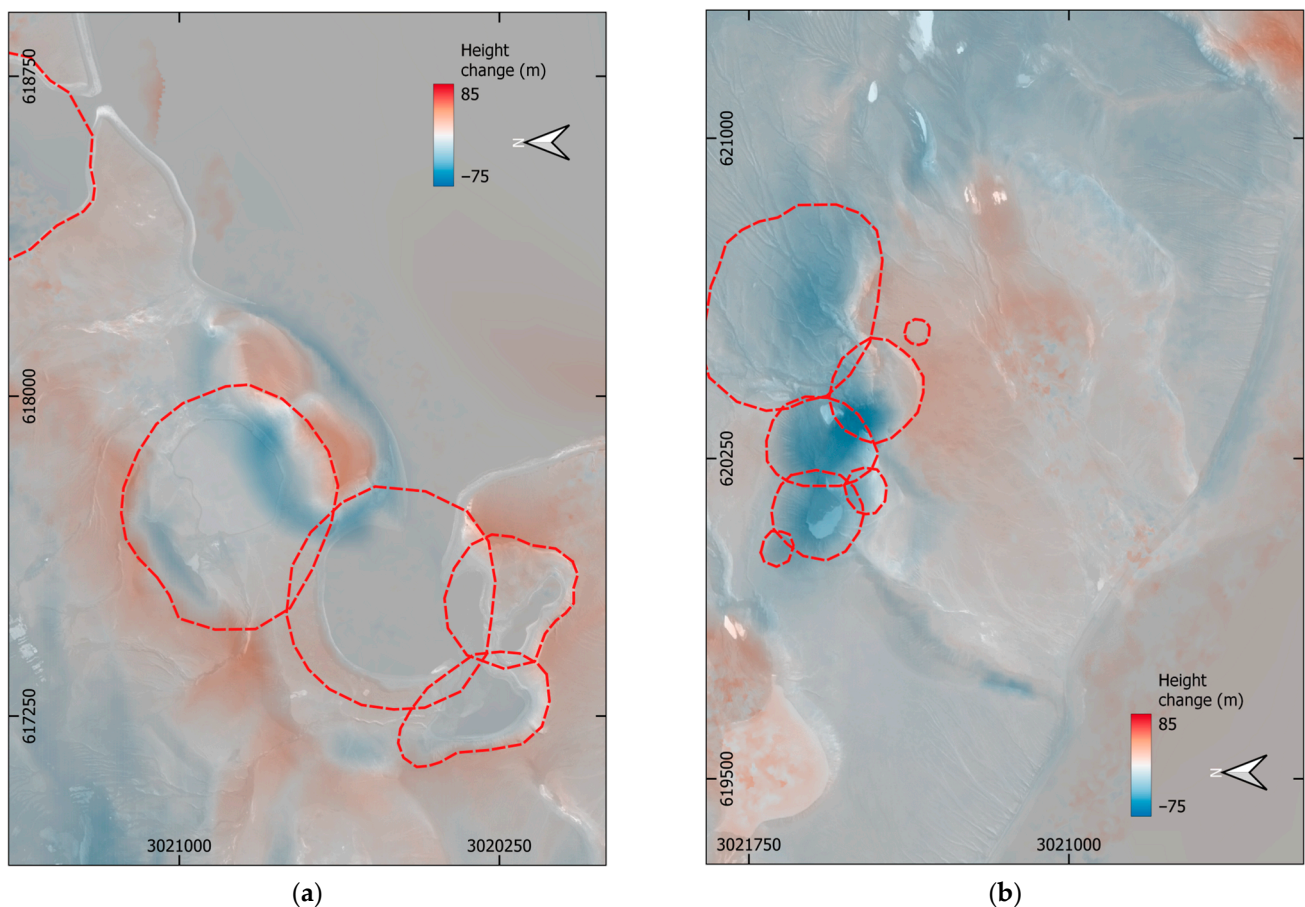


Figure 10. The composition of the 2020 orthographic mosaic in black and white overlapped with 30% transparency to the height differences between the 1968 and REMA digital elevation models in colour from WGS84–UTM20S, and red dashed lines delimiting main volcanic structures. (a) The collapse of the northwest face of the 1967 scoria cones and its annexation and maar craters. (b) The set of craters formed in 1970, one of which with a depth of about 85 m and a crater diameter of 300 m covered by an alluvial fan.

5. Conclusions

The SfM–MvS near-automated digital strategies favour the recovery of historical aerial frames to promote studies from such raw data and extend the time span to those times when no remote sensing satellites were available, producing images with similar resolution and precision. Historical aerial frames were taken of Deception Island, which are not always completely without clouds, like satellite imagery. From those without clouds, two new orthographic mosaics and associated digital elevation models were generated by revising images from 1956 and 1968. Another orthographic mosaic of Kompsat-3 satellite images for 2020 was produced and the REMA digital elevation model was accessed. The general rms of all orthographic mosaics with respect to phase-differential GNSS was 1.8 m and 1.7 m in easting and northing, respectively. Hence, horizontal differences should be statistically significant with a 95% confidence level above 4.8 m, being less in features having expected immobility. Increasing the degree of overlap with added sets of aerial frames from different dates, where no geomorphological changes were expected, increased the precision of both the digital elevation model and the orthographic mosaic.

From the orthographic mosaics, it was possible to visualise the emplacement of two scoria cones and one maar crater aligned NE–SW near the northern shore as well as a prominent crater on land east of those after the 1967 eruption. Along these emerging volcanic structures formation ash was emitted that covered Deception Island’s inner coast and all of Mount Pond, being mainly driven southeastward [31]. This volcanic ash dispersed

over Deception Island covering an area of about 104.6 km². The thickness of volcanic ash can be depicted on the 1968 orthographic mosaic covering man-made structures at the Argentinean, Chilean, and British bases, at heights comparable to about 3 to 5 m (Figure 4) [50]. If an average ash thickness over Deception Island of 1 m is assumed, then a volume of at least 0.104 km³ must be added to the previously calculated volume of erupted ash in 1967 (Table 2), varying from 3 to 5 m [50] at the Argentinean and Chilean bases to about 0.5 m at the British base. Ashfall outside of Deception Island [52] was not calculated in this study.

Table 2. The comparison of erupted ash calculated volumes. The underwater volume was estimated for an average depth of about 10 m, shown in parentheses. The estimated volume uncertainty is from height uncertainty and land area. Negative values represent excavated erupted ash, and positive values represent deposited erupted ash.

| Zone | Heights (m) | Partial Volume (km ³) | Total Volume (km ³) | Previous Volume (km ³) |
|---------------------------------|-------------|-----------------------------------|---------------------------------|------------------------------------|
| 1967 scoria cones (Telefon Bay) | - 53 | -0.002 +0.007 (+0.003) | 0.012 ± 0.003 | |
| 1967 crater (Land Craters) | - 151 | -0.017 +0.028 | 0.044 ± 0.007 | 0.05 [29] 0.057 [12] |
| 1967 ashfall (Deception Island) | 1 | +0.104 | 0.104 | |
| 1970 maar (Telefon Bay) | - | -0.003 +0.016 (+0.008) | 0.027 ± 0.005 | 0.04 [29] 0.053 [12] |
| 1970 craters (Land Craters) | 85 | -0.011 +0.011 | 0.022 ± 0.007 | |

The 1969 floods and the 1970 maars and craters were the main volcanic events of the next two phases of the 1967–1970 eruptive sequence. The orthographic mosaics similarly illustrate the destruction of the Chilean and British bases due to the 1967 ashfall and the 1969 floods [32], particularly visible in the 2020 orthographic mosaic. Visible man-made structures still in place, such as the British base silos and the Argentinean base buildings, were used for matching. The thickness of ashfall makes these structures identifiable, but they are geometrically less clear on the 1968 orthographic mosaic (Figures 6 and 8).

Even if height differences should be statistically significant with a 95% confidence level only above 8.4 m among the 1956 and 1968 digital elevation models, the computed volume of erupted ash of about 0.056 km³ agrees with those of previous studies of 0.05 km³ [29] and 0.057 km³ [12], yet only in the area where the volcanic structures developed then. Since REMA has submeter uncertainties [40], height differences should be statistically significant with a 95% confidence level only above 7.4 m between the 1968 and REMA digital elevation models. The erupted ash volume from 1969 was not possible to compute on these new cartographic products. In 1970, the volume of erupted ash, 0.49 km³, within the areas of the developed volcanic structures also agrees with the previous values of 0.04 km³ [29] and 0.053 km³ [12].

The erupted ash volumes are from the areas with previous cartographic products, mainly from the Deception Island northern sector close to the submerged caldera coast. In this study, the estimated volume of 0.104 km³ covering Deception Island after the 1967 eruption was added. In addition, in 1970, the volume of excavated ash was not totally computed with these cartographic products. In fact, the 2020 orthographic mosaic and the REMA digital elevation model register the height of an alluvial fan that completely fills and covers the 100 m depth and 300 m diameter crater of 1970 on land [31], perhaps favoured in recent years by the rise in mean annual atmospheric temperature and snowfall [53].

Therefore, these new orthographic mosaics have provided the opportunity to study the geomorphological, man-made structure, and biological changes on Deception Island with metric accuracy. The basis for generating additional orthographic mosaics from available

sets of historical aerial frames and successive satellite imagery of Deception Island was also established.

Author Contributions: Conceptualization, G.P.; formal analysis, G.P.; funding acquisition, M.B. and G.V.; methodology, G.P.; resources, G.P., C.T., M.B., G.G. and G.V.; validation, G.P.; visualization, G.P., C.T., G.G. and G.V.; writing—original draft, G.P.; writing—review and editing, G.P., C.T. and G.V. All authors have read and agreed to the published version of the manuscript.

Funding: This research was funded by the Spanish Ministry of Economy and Competitiveness on “Modelización y seguimiento de procesos geodinámicos activos mediante deformación geodésica GNSS en diferentes escenarios (Antártida, Andalucía oc. y Centroamérica)” (CTM2017-84210-R), the Portuguese Science and Technology Foundation on “Permafrost e alterações climáticas na Península Antártica” (PTDC/AAG-GLO/3908/2012), and by the Portuguese Polar Program.

Data Availability Statement: Not applicable.

Acknowledgments: The British Antarctic Survey (BAS) and United States Geological Survey (USGS) are acknowledged for proving access to FIDASE historical aerial frames downloaded from Earth Explorer. The University of Minnesota is acknowledged for access to the REMA digital elevation model. The Laboratorio de Astronomía, Geodésia y Cartografía (LAGC) and the Spanish Centro Geográfico del Ejército (CGE) are acknowledged for the ground control GNSS measured points. The reviewers are acknowledged for their comments and suggestions.

Conflicts of Interest: The authors declare no conflict of interest. The founding sponsors had no role in the design of the study; in the collection, analysis, or interpretation of data; in the writing of the manuscript, or in the decision to publish the results.

Appendix A

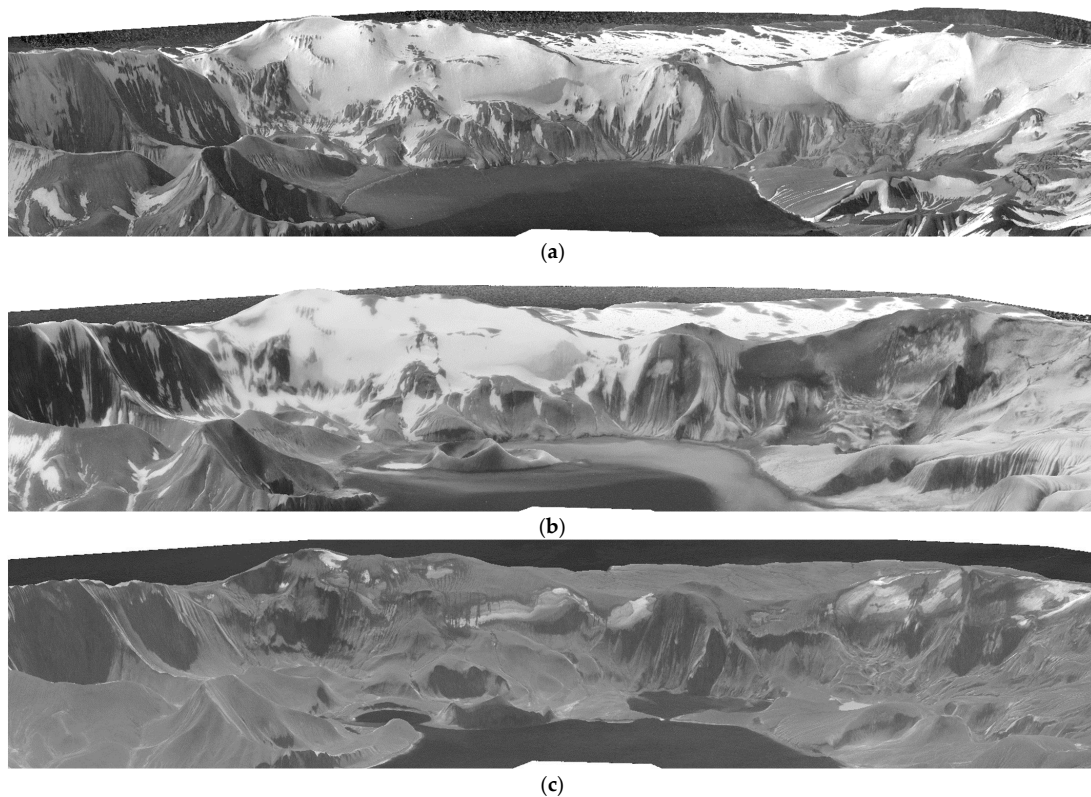


Figure A1. Telefon Bay perspective view based on 1956 (a), 1968 (b), and 2020 (c) orthographic mosaics and digital elevation models (height exaggeration by 3). Includes material ©KARI 2020, copyrighted distribution (SI Imaging Services, Republic of Korea), all rights reserved.

Appendix B

Table A1. Coordinates of ground control points in WGS84–UTM20S.

| GNSS | | 1956 | | 1968 | | 2020 | |
|-------------|---------------|-------------|---------------|-------------|---------------|-------------|---------------|
| X (m) | Y (m) |
| 616,400.428 | 3,014,773.067 | - | - | 616,399.353 | 3,014,773.858 | 616,401.355 | 3,014,774.258 |
| 616,398.094 | 3,014,772.781 | - | - | 616,396.950 | 3,014,773.698 | 616,398.312 | 3,014,774.418 |
| 616,397.882 | 3,014,775.195 | - | - | 616,396.790 | 3,014,776.261 | 616,398.152 | 3,014,777.462 |
| 616,548.713 | 3,014,881.153 | - | - | - | - | 616,548.803 | 3,014,881.260 |
| 616,571.922 | 3,014,909.085 | - | - | 616,571.709 | 3,014,909.452 | 616,571.709 | 3,014,908.331 |
| 616,573.190 | 3,014,912.727 | - | - | 616,572.991 | 3,014,912.816 | 616,572.671 | 3,014,912.015 |
| 616,570.457 | 3,014,913.903 | - | - | 616,570.268 | 3,014,913.457 | 616,569.947 | 3,014,912.976 |
| 616,569.054 | 3,014,909.696 | - | - | 616,568.986 | 3,014,910.093 | 616,568.506 | 3,014,908.812 |
| 616,551.933 | 3,014,909.751 | - | - | 616,552.167 | 3,014,909.212 | 616,551.046 | 3,014,908.411 |
| 616,547.347 | 3,014,906.706 | - | - | 616,548.002 | 3,014,906.970 | 616,547.041 | 3,014,907.290 |
| 616,541.279 | 3,014,916.869 | 616,539.032 | 3,014,904.407 | 616,539.032 | 3,014,904.567 | 616,538.231 | 3,014,904.887 |
| 616,539.739 | 3,014,909.211 | 616,531.504 | 3,014,906.489 | 616,531.824 | 3,014,906.809 | 616,540.153 | 3,014,908.732 |
| 616,538.606 | 3,014,904.795 | 616,539.833 | 3,014,909.372 | 616,539.833 | 3,014,909.372 | 616,531.664 | 3,014,906.809 |
| 616,531.758 | 3,014,906.453 | 616,541.435 | 3,014,917.061 | 616,541.755 | 3,014,917.381 | 616,541.915 | 3,014,917.061 |
| 616,533.926 | 3,014,915.593 | 616,534.521 | 3,014,915.284 | 616,534.256 | 3,014,915.813 | 616,533.992 | 3,014,915.416 |
| 616,529.113 | 3,014,912.659 | 616,530.023 | 3,014,912.109 | 616,529.626 | 3,014,913.035 | 616,529.097 | 3,014,912.770 |
| 616,526.710 | 3,014,918.052 | 616,527.245 | 3,014,917.665 | 616,529.097 | 3,014,911.976 | 616,526.186 | 3,014,918.062 |
| 616,537.317 | 3,014,924.062 | 616,537.431 | 3,014,923.486 | 616,534.653 | 3,014,916.077 | 616,537.299 | 3,014,923.883 |
| 616,526.149 | 3,014,928.643 | 616,525.922 | 3,014,928.248 | 616,526.848 | 3,014,918.459 | 616,526.054 | 3,014,928.645 |
| 616,545.441 | 3,014,921.745 | 616,545.633 | 3,014,921.369 | 616,545.369 | 3,014,922.031 | 616,544.972 | 3,014,921.898 |
| 616,550.641 | 3,014,924.271 | 616,550.793 | 3,014,924.015 | 616,550.396 | 3,014,924.147 | 616,550.528 | 3,014,924.809 |
| 616,551.420 | 3,014,929.410 | 616,551.057 | 3,014,929.571 | 616,552.248 | 3,014,932.878 | 616,551.057 | 3,014,929.703 |
| 616,552.423 | 3,014,932.971 | 616,552.248 | 3,014,933.275 | 616,552.248 | 3,014,932.878 | 616,552.248 | 3,014,932.878 |
| 616,549.195 | 3,014,934.023 | 616,548.676 | 3,014,933.540 | 616,548.941 | 3,014,934.201 | 616,548.941 | 3,014,933.672 |
| 616,538.748 | 3,014,935.236 | 616,539.151 | 3,014,934.863 | 616,539.151 | 3,014,934.995 | 616,538.622 | 3,014,935.127 |
| 616,538.957 | 3,014,930.255 | 616,538.886 | 3,014,929.703 | 616,539.019 | 3,014,930.100 | 616,538.754 | 3,014,929.968 |
| 616,555.562 | 3,014,941.081 | 616,555.291 | 3,014,940.816 | 616,555.555 | 3,014,940.684 | 616,555.687 | 3,014,941.345 |
| 616,557.280 | 3,014,946.949 | 616,557.143 | 3,014,946.372 | 616,556.878 | 3,014,946.108 | 616,557.143 | 3,014,946.108 |
| 616,551.016 | 3,014,942.213 | 616,550.660 | 3,014,942.271 | 616,550.396 | 3,014,941.874 | 616,550.925 | 3,014,942.139 |
| 616,552.956 | 3,014,949.106 | 616,552.248 | 3,014,948.489 | 616,552.248 | 3,014,948.357 | 616,552.645 | 3,014,948.753 |
| 616,541.318 | 3,014,945.563 | 616,541.665 | 3,014,945.182 | 616,541.268 | 3,014,945.049 | 616,541.797 | 3,014,945.314 |
| 616,543.624 | 3,014,951.815 | 616,543.252 | 3,014,951.002 | 616,543.517 | 3,014,951.002 | 616,543.649 | 3,014,951.532 |
| 616,548.336 | 3,014,992.703 | 616,548.544 | 3,014,991.881 | 616,547.485 | 3,014,992.277 | 616,548.147 | 3,014,992.145 |
| 616,721.362 | 3,015,040.519 | - | - | 616,721.052 | 3,015,040.961 | 616,720.787 | 3,015,041.490 |
| 616,700.576 | 3,015,041.205 | 616,701.208 | 3,015,040.035 | 616,700.811 | 3,015,040.299 | 616,699.224 | 3,015,040.696 |
| 616,666.176 | 3,015,041.956 | 616,667.077 | 3,015,041.225 | 616,667.342 | 3,015,041.754 | 616,666.548 | 3,015,041.622 |
| 616,654.683 | 3,015,042.262 | 616,655.303 | 3,015,046.914 | 616,654.774 | 3,015,046.517 | 616,654.642 | 3,015,047.178 |
| 616,668.352 | 3,015,075.181 | 616,669.326 | 3,015,073.901 | 616,669.061 | 3,015,074.960 | 616,668.665 | 3,015,075.489 |
| 622,202.551 | 3,019,264.360 | 622,201.896 | 3,019,263.711 | 622,201.234 | 3,019,263.314 | 622,201.499 | 3,019,263.578 |
| 622,196.579 | 3,019,264.044 | 622,194.487 | 3,019,263.843 | 622,195.546 | 3,019,263.049 | 622,195.017 | 3,019,263.446 |
| 622,195.831 | 3,019,281.200 | 622,194.223 | 3,019,281.173 | 622,194.752 | 3,019,280.776 | 622,195.149 | 3,019,280.512 |
| 622,194.891 | 3,019,289.453 | 622,194.091 | 3,019,289.111 | 622,194.487 | 3,019,288.449 | 622,194.620 | 3,019,289.243 |
| 622,194.726 | 3,019,291.951 | 622,194.091 | 3,019,292.550 | 622,194.620 | 3,019,291.624 | 622,194.620 | 3,019,291.492 |
| 622,197.156 | 3,019,291.930 | 622,197.266 | 3,019,292.418 | 622,197.001 | 3,019,291.624 | 622,197.001 | 3,019,291.624 |
| 622,197.093 | 3,019,289.361 | 622,197.398 | 3,019,289.508 | 622,197.133 | 3,019,289.375 | 622,197.001 | 3,019,289.375 |
| 623,371.825 | 3,014,483.666 | 623,371.784 | 3,014,484.410 | 623,372.677 | 3,014,482.822 | 623,371.288 | 3,014,484.013 |
| 623,380.936 | 3,014,487.817 | 623,381.706 | 3,014,487.188 | 623,383.591 | 3,014,487.386 | 623,380.813 | 3,014,488.577 |
| 623,428.358 | 3,014,507.872 | 623,428.537 | 3,014,507.428 | 623,429.232 | 3,014,507.627 | 623,429.232 | 3,014,507.825 |
| 623,440.511 | 3,014,513.288 | 623,440.642 | 3,014,512.786 | 623,441.336 | 3,014,513.382 | 623,440.543 | 3,014,513.580 |
| 623,438.680 | 3,014,515.133 | 623,438.658 | 3,014,514.771 | 623,438.558 | 3,014,515.366 | 623,438.757 | 3,014,514.969 |
| 623,437.702 | 3,014,517.809 | 623,437.665 | 3,014,517.549 | 623,437.765 | 3,014,518.541 | 623,437.765 | 3,014,517.747 |
| 623,429.404 | 3,014,514.572 | 623,428.140 | 3,014,514.175 | 623,429.033 | 3,014,514.969 | 623,429.827 | 3,014,514.771 |
| 623,430.354 | 3,014,511.936 | 623,428.934 | 3,014,511.596 | 623,430.621 | 3,014,511.794 | 623,430.422 | 3,014,511.794 |
| 623,394.171 | 3,014,576.698 | 623,394.307 | 3,014,576.981 | 623,394.604 | 3,014,576.882 | 623,394.704 | 3,014,577.080 |
| 623,393.688 | 3,014,582.304 | 623,393.711 | 3,014,581.148 | 623,393.612 | 3,014,581.842 | 623,394.108 | 3,014,583.430 |
| 623,402.655 | 3,014,583.675 | 623,403.236 | 3,014,583.728 | 623,403.733 | 3,014,583.628 | 623,404.427 | 3,014,584.819 |
| 623,403.574 | 3,014,578.981 | 623,404.030 | 3,014,578.370 | 623,404.526 | 3,014,578.469 | 623,405.022 | 3,014,580.652 |

References

1. Robertson Maurice, S.D.; Wiens, D.A.; Shore, P.J.; Vera, E.; Dorman, L.M. Seismicity and Tectonics of the South Shetland Islands and Bransfield Strait from a Regional Broadband Seismograph Deployment. *J. Geophys. Res. Solid Earth* **2003**, *108*. [[CrossRef](#)]
2. Taylor, F.W.; Bevis, M.G.; Dalziel, I.W.D.; Smalley, R.; Fröhlich, C.; Kendrick, E.; Foster, J.; Phillips, D.; Gudipati, K. Kinematics and Segmentation of the South Shetland Islands- Bransfield Basin System, Northern Antarctic Peninsula. *Geochem. Geophys. Geosyst.* **2008**, *9*. [[CrossRef](#)]

3. Jin, Y.K.; Lee, J.; Hong, J.K.; Nam, S.H. Is Subduction Ongoing in the South Shetland Trench, Antarctic Peninsula?: New Constraints from Crustal Structures of Outer Trench Wall. *Geosci. J.* **2009**, *13*, 59–67. [[CrossRef](#)]
4. Maestro, A.; Somoza, L.; Rey, J.; Martínez-Frías, J.; López-Martínez, J. Active Tectonics, Fault Patterns, and Stress Field of Deception Island: A Response to Oblique Convergence between the Pacific and Antarctic Plates. *J. S. Am. Earth Sci.* **2007**, *23*, 256–268. [[CrossRef](#)]
5. Solari, M.A.; Hervé, F.; Martinod, J.; Le Roux, J.P.; Ramírez, L.E.; Palacios, C. Geotectonic Evolution of the Bransfield Basin, Antarctic Peninsula: Insights from Analogue Models. *Antarct. Sci.* **2008**, *20*, 185–196. [[CrossRef](#)]
6. Berrocoso, M.; Fernández-Ros, A.; Prates, G.; García, A.; Kraus, S. Geodetic Implications on Block Formation and Geodynamic Domains in the South Shetland Islands, Antarctic Peninsula. *Tectonophysics* **2016**, *666*, 211–219. [[CrossRef](#)]
7. González-Casado, J.M.; Giner-Roles, J.L.; López-Martínez, J. Bransfield Basin, Antarctic Peninsula: Not a normal backarc basin. *Geology* **2000**, *28*, 1043–1046. [[CrossRef](#)]
8. Fretzdorff, S.; Worthington, T.J.; Haase, K.M.; Hékinian, R.; Franz, L.; Keller, R.A.; Stoffers, P. Magmatism in the Bransfield Basin: Rifting of the South Shetland Arc? *J. Geophys. Res. Solid Earth* **2004**, *109*. [[CrossRef](#)]
9. Smellie, J.L. Lithostratigraphy and volcanic evolution of Deception Island, South Shetland Islands. *Antarct. Sci.* **2001**, *13*, 188–209. [[CrossRef](#)]
10. Torrecillas, C.; Berrocoso, M.; Felpeto, A.; Torrecillas, M.D.; García, A. Reconstructing Palaeo-Volcanic Geometries Using a Geodynamic Regression Model (GRM): Application to Deception Island Volcano (South Shetland Islands, Antarctica). *Geomorphology* **2013**, *182*, 79–88. [[CrossRef](#)]
11. Smellie, J.L.; López-Martínez, J.; Headland, R.K.; Hernández-Cifuentes, F.; Maestro, A.; Miller, I.L.; Rey, J.; Serrano, E.; Somoza, L.; Thomson, M.R.A. Geology and geomorphology of Deception Island. In *BAS GEOMAP Series*; British Antarctic Survey: Cambridge, UK, 2002; Sheet 6A and 6B, 1:25 000, with supplementary text, 3 pp.
12. Torrecillas, C.; Berrocoso, M.; Pérez-López, R.; Torrecillas, M.D. Determination of Volumetric Variations and Coastal Changes Due to Historical Volcanic Eruptions Using Historical Maps and Remote-Sensing at Deception Island (West-Antarctica). *Geomorphology* **2012**, *136*, 6–14. [[CrossRef](#)]
13. Pedrazzi, D.; Németh, K.; Geyer, A.; Álvarez-Valero, A.M.; Aguirre-Díaz, G.; Bartolini, S. Historic Hydrovolcanism at Deception Island (Antarctica): Implications for Eruption Hazards. *Bull. Volcanol.* **2018**, *80*, 11. [[CrossRef](#)]
14. Carmona, E.; Almendros, J.; Serrano, I.; Stich, D.; Ibáñez, J.M. Results of Seismic Monitoring Surveys of Deception Island Volcano, Antarctica, from 1999–2011. *Antarct. Sci.* **2012**, *24*, 485–499. [[CrossRef](#)]
15. Ortiz, R.; García, A.; Aparicio, A.; Blanco, I.; Felpeto, A.; Del Rey, R.; Villegas, M.; Ibáñez, J.M.; Morales, J.; Del Pezzo, E.; et al. Monitoring of the volcanic activity of Deception Island, South Shetland Islands, Antarctica (1986–1995). In *The Antarctic Region: Geological Evolution and Processes*; Ricci, C.A., Ed.; Terra Antarctica Publication L: Siena, Italy, 1997; pp. 1071–1076.
16. Ibáñez, J.M.; Del Pezzo, E.; Almendros, J.; La Rocca, M.; Alguacil, G.; Ortiz, R.; García, A. Seismovolcanic Signals at Deception Island Volcano, Antarctica: Wave Field Analysis and Source Modeling. *J. Geophys. Res. Solid Earth* **2000**, *105*, 13905–13931. [[CrossRef](#)]
17. Ibáñez, J.M.; Carmona, E.; Almendros, J.; Saccorotti, G.; Del Pezzo, E.; Abril, M.; Ortiz, R. The 1998–1999 Seismic Series at Deception Island Volcano, Antarctica. *J. Volcanol. Geotherm. Res.* **2003**, *128*, 65–88. [[CrossRef](#)]
18. Berrocoso, M.; Prates, G.; Fernández-Ros, A.; Peci, L.M.; de Gil, A.; Rosado, B.; Páez, R.; Jigena, B. Caldera Unrest Detected with Seawater Temperature Anomalies at Deception Island, Antarctic Peninsula. *Bull. Volcanol.* **2018**, *80*, 41. [[CrossRef](#)]
19. Moreno-Vacas, A.; Almendros, J. On the Origin of Recent Seismic Unrest Episodes at Deception Island Volcano, Antarctica. *J. Volcanol. Geotherm. Res.* **2021**, *419*, 107376. [[CrossRef](#)]
20. Núñez-Regodón, J. Diario de Operaciones 2019/2020 del Ejército de Tierra de España. 2020. Available online: <https://ejercito.defensa.gob.es/unidades/Antartica/antartica/index.html> (accessed on 24 February 2023).
21. García, A.; Blanco, I.; Torta, J.M.; Astiz, M.M.; Ibáñez, J.M.; Ortiz, R. A Search for the Volcanomagnetic Signal at Deception Volcano (South Shetland I., Antarctica). *Ann. Geophys.* **1997**, *40*. [[CrossRef](#)]
22. Zandomenighi, D.; Barclay, A.; Almendros, J.; Godoy, J.M.I.; Wilcock, W.S.D.; Ben-Zvi, T. Crustal Structure of Deception Island Volcano from P Wave Seismic Tomography: Tectonic and Volcanic Implications. *J. Geophys. Res. Solid Earth* **2009**, *114*. [[CrossRef](#)]
23. Prudencio, J.; De Siena, L.; Ibáñez, J.M.; Del Pezzo, E.; García-Yeguas, A.; Díaz-Moreno, A. The 3D Attenuation Structure of Deception Island (Antarctica). *Surv. Geophys.* **2015**, *36*, 371–390. [[CrossRef](#)]
24. Padrón, E.; Hernández, P.A.; Carmona, E.; Pérez, N.M.; Melián, G.; Sumino, H.; Almendros, J.; Kusakabe, M.; Wakita, H.; Padilla, G.D. Geochemical Evidence of Different Sources of Long-Period Seismic Events at Deception Volcano, South Shetland Islands, Antarctica. *Antarct. Sci.* **2015**, *27*, 557–565. [[CrossRef](#)]
25. Bartolini, S.; Geyer, A.; Martí, J.; Pedrazzi, D.; Aguirre-Díaz, G. Volcanic Hazard on Deception Island (South Shetland Islands, Antarctica). *J. Volcanol. Geotherm. Res.* **2014**, *285*, 150–168. [[CrossRef](#)]
26. Pedrazzi, D.; Aguirre-Díaz, G.; Bartolini, S.; Martí, J.; Geyer, A. The 1970 Eruption on Deception Island (Antarctica): Eruptive Dynamics and Implications for Volcanic Hazards. *J. Geol. Soc. Lond.* **2014**, *171*, 765–778. [[CrossRef](#)]

27. Aristarain, A.J.; Delmas, R. First Glaciological Studies on the James Ross Island Ice Cap, Antarctic Peninsula. *J. Glaciol.* **1981**, *27*, 371–379. [[CrossRef](#)]
28. Pallàs, R.; Smellie, J.L.; Casas, J.M.; Calvet, J. Using Tephrochronology to Date Temperate Ice: Correlation between Ice Tephra on Livingston Island and Eruptive Units on Deception Island Volcano (South Shetland Islands, Antarctica). *Holocene* **2001**, *11*, 149–160. [[CrossRef](#)]
29. Roobol, M.J. The Volcanic Hazard at Deception Island, South Shetland Islands. *Br. Antarct. Surv. Bull.* **1982**, *51*, 237–245.
30. Baker, P.; Roobol, M.; McReath, M.; Harvey, M.; Davies, T. The geology of the South Shetland Islands. Volcanic evolution of Deception Island: Introduction. In *British Antarctic Survey Scientific Reports*; British Antarctic Survey: Cambridge, UK, 1975; Volume 78.
31. Brecher, H.H. Photogrammetric Maps of a Volcanic Eruption Area, Deception Island, Antarctica. In *Institute of Polar Studies Report No. 52*; Research Foundation and the Institute of Polar Studies, The Ohio State University: Columbus, OH, USA, 1975; Volume 52, 10p.
32. Smellie, J.L. The 1969 Subglacial Eruption on Deception Island (Antarctica): Events and Processes during an Eruption beneath a Thin Glacier and Implications for Volcanic Hazards. *Geol. Soc. London, Spec. Publ.* **2002**, *202*, 59–79. [[CrossRef](#)]
33. Berrocoso, M.; Torrecillas, C.; Jigena, B.; Fernández-Ros, A. Determination of Geomorphological and Volumetric Variations in the 1970 Land Volcanic Craters Area (Deception Island, Antarctica) from 1968 Using Historical and Current Maps, Remote Sensing and GNSS. *Antarct. Sci.* **2012**, *24*, 367–376. [[CrossRef](#)]
34. Diefenbach, A.K.; Crider, J.G.; Schilling, S.P.; Dzurisin, D. Rapid, Low-Cost Photogrammetry to Monitor Volcanic Eruptions: An Example from Mount St. Helens, Washington, USA. *Bull. Volcanol.* **2012**, *74*, 579–587. [[CrossRef](#)]
35. Gomez, C. Digital Photogrammetry and GIS-Based Analysis of the Bio-Geomorphological Evolution of Sakurajima Volcano, Diachronic Analysis from 1947 to 2006. *J. Volcanol. Geotherm. Res.* **2014**, *280*, 1–13. [[CrossRef](#)]
36. Dvigalo, V.; Shevchenko, A.; Svirid, I. Photogrammetric Survey in Volcanology: A Case Study for Kamchatka Active Volcanoes. In *Updates in Volcanology—From Volcano Modelling to Volcano Geology*; InTechOpen: London, UK, 2016.
37. Gomez, C.; Setiawan, M.A.; Listyaningrum, N.; Wibowo, S.B.; Hadmoko, D.S.; Suryanto, W.; Darmawan, H.; Bradak, B.; Daikai, R.; Sunardi, S.; et al. LiDAR and UAV SfM-MVS of Merapi Volcanic Dome and Crater Rim Change from 2012 to 2014. *Remote Sens.* **2022**, *14*, 5193. [[CrossRef](#)]
38. Román, A.; Tovar-Sánchez, A.; Roque-Atienza, D.; Huertas, I.E.; Caballero, I.; Fraile-Nuez, E.; Navarro, G. Unmanned Aerial Vehicles (UAVs) as a Tool for Hazard Assessment: The 2021 Eruption of Cumbre Vieja Volcano, La Palma Island (Spain). *Sci. Total Environ.* **2022**, *843*, 157092. [[CrossRef](#)]
39. Knuth, F.; Shean, D.; Bhushan, S.; Schwab, E.; Alexandrov, O.; McNeil, C.; Dehecq, A.; Florentine, C.; O’Neel, S. Historical Structure from Motion (HSfM): Automated processing of historical aerial photographs for long-term topographic change analysis. *Remote Sens. Environ.* **2023**, *285*, 113379. [[CrossRef](#)]
40. Howat, I.M.; Porter, C.; Smith, B.E.; Noh, M.J.; Morin, P. The Reference Elevation Model of Antarctica. *Cryosphere* **2019**, *13*, 665–674. [[CrossRef](#)]
41. Kääb, A.; Vollmer, M. Surface Geometry, Thickness Changes and Flow Fields on Creeping Mountain Permafrost: Automatic Extraction by Digital Image Analysis. *Permafr. Periglac. Process.* **2000**, *11*, 315–326. [[CrossRef](#)]
42. Westoby, M.J.; Brasington, J.; Glasser, N.F.; Hambrey, M.J.; Reynolds, J.M. “Structure-from-Motion” Photogrammetry: A Low-Cost, Effective Tool for Geoscience Applications. *Geomorphology* **2012**, *179*, 300–314. [[CrossRef](#)]
43. Snavely, N.; Seitz, S.M.; Szeliski, R. Modeling the World from Internet Photo Collections. *Int. J. Comput. Vis.* **2008**, *80*, 189–210. [[CrossRef](#)]
44. Furukawa, Y.; Ponce, J. Accurate, Dense, and Robust Multi-View Stereopsis. In Proceedings of the IEEE Computer Society Conference on Computer Vision and Pattern Recognition, Minneapolis, MN, USA, 17–22 June 2007. [[CrossRef](#)]
45. Tao, C.V.; Hu, Y. A Comprehensive Study of the Rational Function Model for Photogrammetric Processing. *Photogramm. Eng. Remote Sens.* **2001**, *67*, 1347–1358.
46. Marí, R.; de Franchis, C.; Meinhardt-Llopis, E.; Anger, J.; Facciolo, G. A Generic Bundle Adjustment Methodology for Indirect RPC Model Refinement of Satellite Imagery. *Image Process. Line* **2021**, *11*, 344–373. [[CrossRef](#)]
47. Lillesand, T.; Kiefer, R.W.; Chipman, J. *Remote Sensing and Image Interpretation*, 7th ed.; Wiley: Hoboken, NJ, USA, 2015; ISBN 9781118919453.
48. Jigena, B.; Berrocoso, M.; Torrecillas, C.; Vidal, J.; Barbero, I.; Fernandez-Ros, A. Determination of an Experimental Geoid at Deception Island, South Shetland Islands, Antarctica. *Antarct. Sci.* **2016**, *28*, 277–292. [[CrossRef](#)]
49. Torrecillas, C.; Berrocoso, M.; García-García, A. The Multidisciplinary Scientific Information Support System (SIMAC) for Deception Island. In *Antarctica: Contributions to Global Earth Sciences*; Springer: Berlin/Heidelberg, Germany, 2006.
50. Roobol, M.J. A model for the eruptive mechanism of Deception Island from 1820 to 1970. *Br. Antarct. Surv. Bull.* **1979**, *49*, 137–156.
51. Flexas, M.M.; Arias, M.R.; Ojeda, M.A. Hydrography and Dynamics of Port Foster, Deception Island, Antarctica. *Antarct. Sci.* **2017**, *29*, 83–93. [[CrossRef](#)]

52. Hopfenblatt, J.; Geyer, A.; Aulinas, M.; Álvarez-Valero, A.M.; Sánchez, A.P.; Giral, S.; Smellie, J.L. DecTephra: A New Database of Deception Island's Tephra Record (Antarctica). *J. Volcanol. Geotherm. Res.* **2022**, *425*, 107516. [[CrossRef](#)]
53. Oliva, M.; Navarro, F.; Hrbáček, F.; Hernández, A.; Nývlt, D.; Pereira, P.; Ruiz-Fernández, J.; Trigo, R. Recent Regional Climate Cooling on the Antarctic Peninsula and Associated Impacts on the Cryosphere. *Sci. Total Environ.* **2017**, *580*, 210–223. [[CrossRef](#)] [[PubMed](#)]

Disclaimer/Publisher's Note: The statements, opinions and data contained in all publications are solely those of the individual author(s) and contributor(s) and not of MDPI and/or the editor(s). MDPI and/or the editor(s) disclaim responsibility for any injury to people or property resulting from any ideas, methods, instructions or products referred to in the content.